Energy Storage Materials 25 (2020) 572–584

Contents lists available at ScienceDirect

Energy Storage Materials

journal homepage: www.elsevier.com/locate/ensm

Electrodeposition of Sb/CNT composite films as anodes for Li- and Na-ion batteries

Maxwell C. Schulze, Ryan M. Belson, Leslie A. Kraynak, Amy L. Prieto *

Department of Chemistry, Colorado State University, Fort Collins, CO, 80523, United States

ARTI CLE INFO

Keywords:
Electrodeposition
CNT composite
Antimony anode
Li-ion battery
Na-ion battery

ABSTRACT

Antimony is a known high capacity anode material for both Li- and Na-ion batteries that has the potential to improve the energy storage density over commercial graphite anode-based Li-ion batteries. As with other high capacity anode materials (such as silicon), the large storage capacity of antimony results in large volume changes of the anode during discharge/recharge cycles. This results in the formation of signi ficant cracking of the anode, causing active material to lose electrical connection to the current collector which, ultimately, causes the cell to fail. To address this type of failure, we incorporate carbon nanotubes into antimony carbon nanotube composite electrodes (Sb/CNT) using a one-step electrodeposition procedure. The advantage of directly depositing functional anodes from solution is that no binders are used and there is no post-processing required. This means that the electrical and mechanical behavior of these materials can be probed directly in functioning battery cells, without the convolution of other materials. The Sb/CNT composite films cycle with higher reversible capacities and for longer than Sb films electrodeposited without CNT's in both the Li-ion and Na-ion cells. Post-cycling characterization of the anodes confirms the ability of the CNT's to keep the anode film more mechanically and electrically connected, despite large volume changes and signi ficant solid-electrolyte-interface layer formation.

1. Introduction

The continuing trends of vehicle electrification and powering electricity grids with intermittent renewable energy sources requires continued development of next generation rechargeable battery technologies [1–3]. There are many known strategies for increasing important performance metrics such as energy/power density, cycle lifetimes, affordability, and safety factors of new battery technologies. However, improving one performance metric often comes at the expense of the others [3]. Thus, additional exploration of emerging battery chemistries can help to identify how different strategies interplay with each other to create battery systems with optimized performance for specific applications.

One of the main strategies for improving energy and power density is to substitute the prototypical graphite anode in rechargeable batteries with alloy anodes that can store greater amounts of Li or Na [4]. Commonly employed alloy anode materials include Si, Ge, Sn, and Sb for Li-ions [4] and P, Sn, Sb for Na-ions [5,6]. These materials suffer from volume changes during (de)alloying with Li or Na that are sufficiently large such that they cause mechanical degradation (cracking) that can disrupt electrical connectivity to the electrodes' current collectors, rendering the isolated material electrochemically inactive. To avoid this mode of electrode degradation, the anode materials can be nanostructured, alloyed with inactive components, and/or formulated with polymer binders and conductive additives.

However, each of those strategies decreases gains in energy density as well as exacerbates a different mode of electrode degradation: excessive buildup of the solid-electrolyte-interface (SEI) layer. The SEI layer forms to passivate any electroactive surfaces exposed to the electrolyte, consuming electrolyte components like Li/Na-salts and solvent molecules [7]. Large surface area (nanostructured) electrodes and newly exposed surfaces (from mechanical degradation) can result in excessive amounts of SEI layer that render intolerable amounts of Li or Na unusable to the cell or impede/block ion movement to and from the electrode [8,9].

As an anode material, Sb exhibits 660 mAh/g storage capacity for Li^{b} and Na^{b} with alloying potentials of ~0.9 V vs. Li/Li ^{b} and ~0.6 V vs. Na/Na^{b}, respectively. The higher redox potentials of Sb compared to graphite (~0.1 V vs. Li/Li ^{b}) do impart an additional safety factor to cells

Abbreviations:SEI, Solid electrolyte interface; CNT, carbon nanotube; CTAB, hexadecyl-trimethylammonium bromide; CE, coulombic efficiency; EDS, energy dispersive X-ray spectroscopy; XPS, X-ray photoelectron spectroscopy; CV, cyclic voltammetry; PXRD, powder X-ray diffraction.

* Corresponding author.
E-mail address: amy.prieto@colostate.edu (A.L. Prieto).

https://doi.org/10.1016/j.ensm.2019.09.025
Received 19 June 2019; Received in revised form 17 September 2019; Accepted 18 September 2019
Available online 22 September 2019

with Sb anodes, as the alloying potentials are sufficiently positive of the Li or Na plating potentials, essentially eliminating the hazard of Li or Na dendrite growth during charging that can be responsible for internal short circuiting and resulting explosions. While this also results in full-cell Li-ion batteries with Sb anodes having lower achievable energy densities than those with graphite anodes, Sb anodes still remain an attractive option for Na-ion batteries. With Sb also being a representative member of high capacity anodes in general, it can serve as a model system to understand their degradation modes with the added bonus of its ability to be easily electrodeposited [10–14].

Producing anode films via electrodeposition ensures good electrical connectivity to metal foil current collectors, and if well controlled, good mechanical adhesion [15]. The technique also allows anodes to be deposited onto non-planar substrates, enabling 3-dimensional battery architectures that are not easily accessible by typical formulation and slurry coating methods of electrode manufacturing [16]. However, many electrode films produced by electrodeposition are susceptible to mechanical degradation because they lack the porosity and mechanical resiliency that give formulated slurry-coated electrodes their good cycling stability. The advantages of electrodeposition can be combined with the mechanical durability of slurry electrodes by developing new electrodeposition procedures that co-deposit the active material with binders or other additives. Carbon nanotubes (CNTs) are a good candidate for co-depositing via electrodeposition [17–20]. Not only could their large aspect ratios provide strong mechanical support to a deposited film over multi-micron length scales, but their electronic conductivity could help keep otherwise mechanically separated portions of active material electrically connected [21]. There are many examples of using CNTs to enhance the performance of battery electrode materials made using electrodeposition [22–24], slurry coating [25], and other methods [24, 26–28]. Additionally, if a suitable aqueous solution is used, electrodeposition allows for completely aqueous production of a functional electrode material, which has been shown to produce significant energy-savings in mass production of that electrode [29].

Herein, we report an aqueous electrodeposition procedure that co-deposits CNTs with an Sb-based active material. This is the first report of an Sb/CNT composite formed via electrodeposition that are cycled without the use of any additional conductive additives or binders. Not only do SEM and XPS analysis confirm the presence of numerous CNTs in the composite film, but the presence of the CNTs also alters the morphology of the deposited film to form a “beads-on-a-string” like porous morphology. We compare the cycling performance of the Sb/CNT composite films to electrodeposited Sb films without CNTs in both Li-ion and Na-ion half cell batteries. The inclusion of the CNTs into the electrodeposited films enhances the performance of the electrodes in both the Li-ion and Na-ion cells, which we attribute to the porous morphology and improved mechanical/electrical connectivity of the Sb/CNT composite films. Post-cycling characterization of the electrode films was used to elucidate specific failure modes of these types of electrodes as well as limitations that need to be addressed before they could be used effectively in full cell batteries. Finally, we show the applicability of this electrodeposition towards another Li-ion alloy system, producing SnSb/CNT films and cycling them in Li-ion half cells.

2. Experimental

2.1. Preparation of electrodeposition solutions

Typical electrodeposition solution batches were made using 200 mM sodium gluconate (20 mmol, 4.363 g, Sigma, >99%), 30 mM hexadecyltrimethylammonium bromide (CTAB, 3 mmol, 1.093 g, Sigma, >98%), 30 mM $SbCl_3$ (3 mmol, 0.684 g, Sigma-Aldrich, anhydrous, >99.0%), and amine functionalized carbon nanotubes (ACNT, excess, cheaptubes.com, >99 wt%, 13–18 nm OD, 3–30μm length, 7.0% 1.5% functional content) in Millipore water (100 mL, 18.2 Mohm). Typically, the sodium gluconate and CTAB were dissolved in the water first, to form a slightly cloudy/opalescent solution. The $SbCl_3$ (and/or $SnCl_2$ Sigma-Aldrich, dihydrate, 98%) was then added and sonicated to first form a cloudy white mixture, which quickly turned to a clear colorless solution upon continued sonication. As a final step (excluded for deposition solutions to be used for depositing films without CNTs), ACNTs were added in excess (5 heaping scoopulas for 100 mL batch) and the mixture sonicated in a bath sonicator for 2 h. The mixture was transferred to centrifuge tubes and centrifuged at 5000 rpm for 5 min to precipitate any unsuspended agglomerations of ACNTs. The homogenous suspension of ACNTs was decanted and used for electrodeposition of the Sb/CNT composite films; the suspended ACNTs remain stably suspended for more than several months.

2.2. Cyclic voltammetry and electrodeposition

A Gamry Reference 3000 potentiostat was used to perform cyclic voltammetry (CV) and electrodepositions. The CVs of the deposition solutions were obtained at 20 mV/s using a three electrode setup with a saturated calomel reference electrode, Pt mesh counter electrode, and Pt working electrode. The electrodepositions were performed using ½” diameter circular disks of either Ni foil (McMaster Carr, 99.0% Ni, Alloy 200/201, 0.001 00thickness) or textured Cu (tCu) foil (Oak-Mitsui, TLB-DS Cu foil) substrate working electrode, stainless steel mesh counter electrode, and a saturated calomel (SCE) reference electrode. Foil substrates were cleaned in a 12 M HCl solution for 15 s followed by rinsing in Millipore water and drying. The substrate foils were then fixed horizontally in an electrodeposition cell where a rubber O-ring defines a 0.713 cm^2 deposition area. The cell fixes the counter electrode ~2 cm above the substrate foil with the reference electrode in between. All electrodepositions were performed at ambient temperature between 21 and 24 C and deposited by holding the potential of the working electrode at 1.05 V vs. SCE until the charge passed equaled 3 C/cm^2 or 10 C/cm^2 for the “high-loading” electrodes. The deposited films were removed from the cell, rinsed with water and then ethanol, then dried in air at ambient temperature.

2.3. Scanning electron microscopy, energy-dispersive X-ray spectroscopy, X-ray diffraction, and X-ray photoelectron spectroscopy

Scanning electron microscopy (SEM) analyses were done using a JEOL JSM-6500F microscope equipped with an Oxford 80 X-MAX (80 mm) SDD energy-dispersive X-ray spectroscopy (EDS) detector. EDS measurements were made at 15 keV and 1kx magnification at three different spots to obtain an average film composition and standard deviation based on the different measurement locations. Quantification of the EDS data was performed using the factory standards included in Oxford AZtec software (3.3 SP1). Samples for cross-sectional imaging were prepared by submerging foil in liquid nitrogen and tearing the foil in half. Powder X-ray diffraction (PXRD) measurements were done using a Bruker D8 Discover DaVinci powder X-ray diffractometer. X-ray photoelectron spectroscopy (XPS) measurements were performed with a Physical Electronics (PHI) 5800 series Multi-Technique ESCA system with a monochromatic Al K α (hν¼ 1486.6 eV) X-ray source operating at 350.0 W. High resolution (HRES) spectra for the elements of interest were collected with a pass energy of 23.5 eV in intervals of 0.100 eV/step over a 0.6 2.0 mm analysis area. After collecting spectra of the pristine films, the samples were sputtered for 60 s using a 3 3 mm 5 keV Ar þ beam to remove adventitious carbon. The binding energies of the HRES spectra were calibrated by shifting the metallic antimony $3d_{5/2}$ peak to 528.0 eV. Peak fitting and quantification of the XPS HRES spectra was performed using CasaXPS (Version 2.3.16). For peak fitting, a nonlinear Shirley background was used, and a 30% Lorentzian/70% Gaussian line shape was used for all peaks except those corresponding to metallic antimony and sp^2 carbon, which were fit with a 30% Lorentzian/70% Gaussian lineshape modified with an exponential blend function. Quantification was based on PHI relative sensitivity factors corrected for

angular distribution.

2.4. Assembly and cycling of half-cell batteries

The ½" diameter electrode foils with the deposited Sb or Sb/CNT composite films were used as working electrodes in two electrode Swagelok cells assembled in an Argon atmosphere glove box. Metallic Li or Na was pressed into the cell with a stainless steel mesh and spring and was used as the reference and counter electrode. The electrolyte used was either 1.0 M $LiPF_6$ in ethylene carbonate (EC):diethylcarbonate (3:7 by volume) or 1 M $NaPF_6$ in EC:dimethylcarbonate:fluorethylenecarbonate (425:425:50 by volume) for the Li- and Na-ion half cells, respectively. The electrolyte was absorbed into a Whatman glass filter sandwiched between two polymer separators in between the electrodes. The assembled cells were allowed to rest for at least 12 h before cycling in order to reach a steady state open circuit voltage (OCV). The battery cells were galvanostatically cycled at ambient temperature using an Arbin Instruments battery tester. The cells were all cycled at a rate of 0.1 mA/mg between 0.01 V and 2.0 V vs. Li/Li^+ or Na/Na^+ unless specified otherwise. The current densities were determined using the gravimetrically measured film loading (~0.9 mg for 3 C/cm^2, ~2.7–3.0 mg for 10 C/cm^2 charge loadings). The cells were disassembled in a delithiated state in air and the anode films rinsed with ethanol and dried before post-cycling SEM imaging.

3. Results and discussion

3.1. Electrodeposition of Sb and Sb/CNT composite films

To co-electrodeposit Sb with CNTs, we modified an aqueous antimony deposition solution by adding a dispersant and amine functionalized CNTs. To facilitate the migration of the CNTs towards the negatively biased substrate and their subsequent inclusion into the electrodeposited film, we rationally designed the solution to impart the suspended CNTs with a positive zeta potential. Using the cationic surfactant CTAB as the dispersant imparts the suspended CNTs with such a positive zeta potential. Additionally, amine functionalization of the CNTs has been shown to result in a positive zeta potential, especially at an acidic pH [30, 31]. The solution composition used for the electrodepositions is shown in Fig. 1a along with CVs that show similar electrochemical behaviors of the solutions with and without suspended CNTs. Fig. 1b shows a PXRD pattern that is representative of films electrodeposited potentiostatically at 1.05 V vs. SCE to 3 C/cm^2 from solutions with and without suspended CNTs onto Ni foil substrates; the resulting films will be referred to as Sb/CNT@Ni and Sb@Ni, respectively. The PXRD pattern shows that both the Sb@Ni and Sb/CNT@Ni films exhibit poor crystallinity, which is typical of films deposited from these types of solutions [14].

Imaging the deposits with SEM reveals significant morphological differences between the Sb@Ni and Sb/CNT@Ni films. Fig. 2a–b shows severe cracking in the Sb@Ni film, indicating significant internal stress, though its surface is smooth and uniform with no dendritic growth. Cross sectional imaging of the Sb@Ni film shown in Fig. 2c provides a film thickness of ~3.5 μm that is dense and free of porosity, while EDS mapping reveals that oxygen is concentrated at the surface of the film. Fig. 2d–e shows less severe cracking of the Sb/CNT@Ni film and rough and porous morphology, with Sb grains nucleating and growing along the length of CNTs to produce nodular features with longer aspect ratios in some cases.Cross sectional imaging of the Sb/CNT@Ni film shown in Fig. 2f provides a film thickness of ~5 μm, while EDS reveals that oxygen is dispersed homogenously through the full thickness of the film, indicating significant porosity throughout where more surfaces can be exposed to and oxidized by air. The error in elemental quantification by EDS shown in Fig. S1 makes the films compositionally indistinguishable, likely because the oxygen and carbon signals are dominated by adventitiously adsorbed species. For this reason, other methods such as XPS needed to be used to confirm the presence of CNTs in the Sb/CNT@Ni film.

To confirm that CNTs are included within the bulk of the Sb/CNT@Ni film, and not just adsorbed onto the surface, XPS analysis was performed before and after sputtering for 60 s. Fig. 3a–b shows high-resolution spectra of the Sb 3d, O 1s, and C 1s binding environments before sputtering, where there is a mixture of Sb metal, Sb oxide, sp^2 carbon from the CNTs, and various C and O environments from adventitiously surface adsorbed species. Fig. 3d–e shows high-resolution spectra of the Sb 3d, O 1s, and C 1s binding environments after 60 s of sputtering. The ratio of Sb:Sb(ox) binding environments has increased compared to the pre-sputtered measurement, indicating that some of the oxide is due to surface oxidation but some is also formed in the bulk of the film during electrodeposition. Additionally, the C and O environments due to adventitiously adsorbed species are gone, leaving only the sp^2 C binding environment from embedded CNTs. This is consistent with CNTs being incorporated throughout the film thickness. Fig. 4 shows the same XPS measurements done on the Sb@Ni film, and the absence of any C binding environment after sputtering confirms that 60 s of sputtering is sufficient to remove adventitiously adsorbed species and that the single C environment in Fig. 3d is due to CNTs embedded within the Sb/CNT@Ni film. It is also clear that there is significant oxide content in the electrodeposited films and Sb_2O_3 is known to participate in conversion reactions with Li and Na [32]. As such, the effects of the presence of Sb_2O_3 in the films are discussed in the supplementary information (see Fig. S1), though the films will be referred to as Sb films throughout the main text.

3.2. Electrochemical performance of Sb and Sb/CNT composite films in Li-ion half cells

The electrochemical performance as Li-ion battery anodes of the Sb@Ni and Sb/CNT@Ni films was assessed by galvanostatically cycling the films in Li-ion half-cells (see Fig. 5). We chose to electrodeposit and cycle the films on Ni instead of Cu, which is typical of anode materials, due to deleterious effects of Cu-Sb interactions. We previously reported

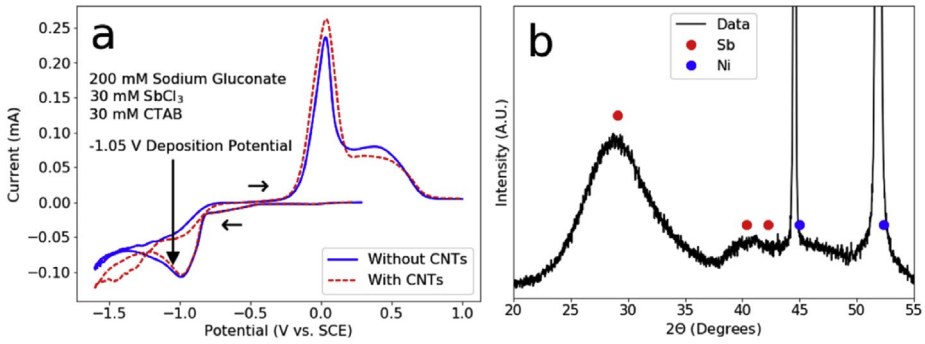

Fig. 1. (a) Cyclic Voltammograms of the listed electrodeposition solution with and without suspended CNTs. (b) A representative powder X-ray diffraction pattern of either the Sb or Sb/CNT composite films electrodeposited @-1.05 V vs. SCE onto Ni foil substrates.

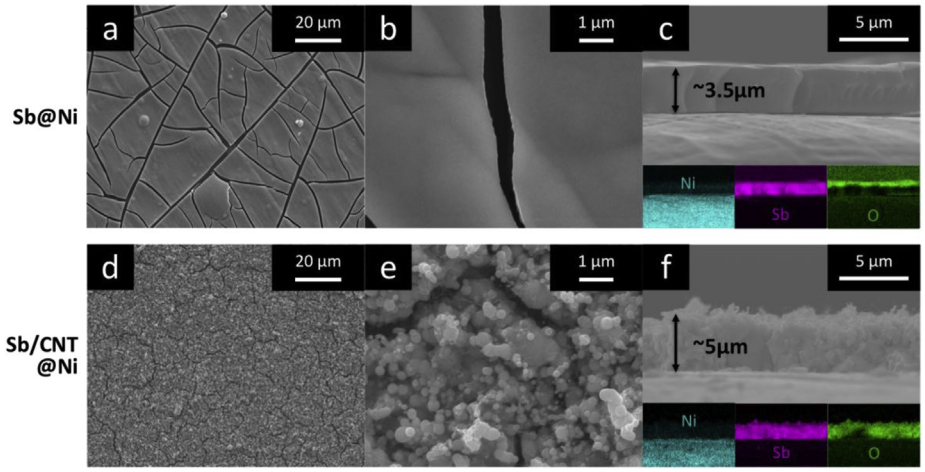

Fig. 2. SEM images of: (a–b) top surface of an Sb@Ni film, (c) cross-section of Sb@Ni film with an EDS map inlay, (d–e) top surface of an Sb/CNT@Ni composite film, (f) cross-section of an Sb/CNT composite film with EDS map inlay.

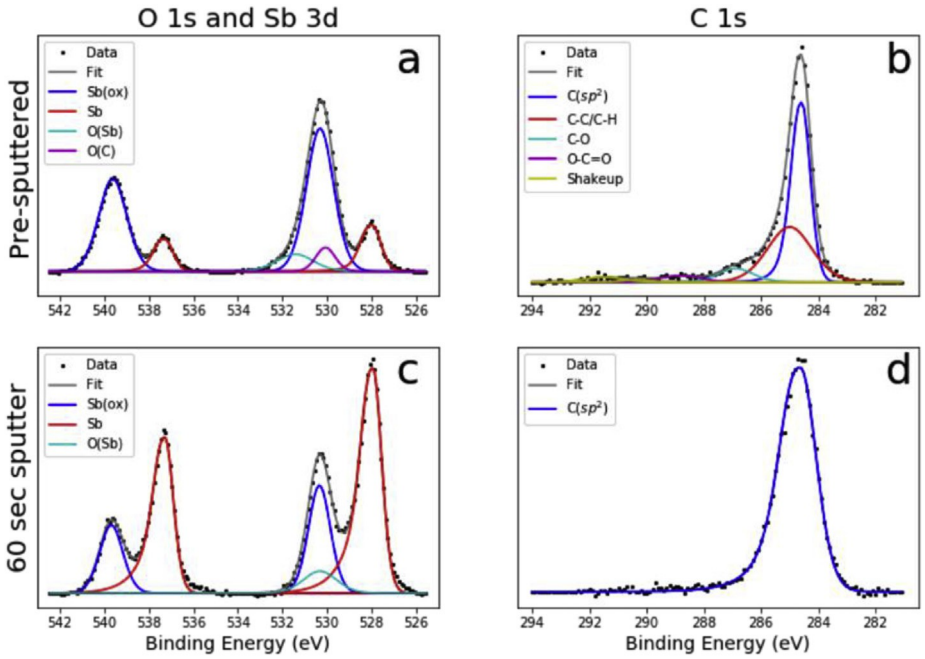

Fig. 3. XPS spectra of Sb/CNT@Ni composite film (a–b) before sputtering and (c–d) after 60 s of sputtering.

on the phenomenon of interdiffusion at Cu-Sb interfaces during cycling in a Li-ion battery that results in void formation at that interface, and is ultimately responsible for delamination and premature failure of the anode material [14]. This remains the case for Sb/CNT@Cu deposits (see Fig. 6). Fig. 5a shows the voltage profiles for (de)lithiation of Sb@Ni and Sb/CNT@Ni, both of which are typical of Sb. The Sb/CNT@Ni film passes more current in the 1.2–2 V vs. Li/Li$^+$ range than the Sb@Ni film, likely due to the larger surface area of the Sb/CNT@Ni film that results in greater amounts of SEI formation/dissolution. Differential capacity analysis of the potential profiles is shown for the (de)lithiation potential regions in Fig. 5b–c. During the lithiation of both films, it is evident that there are two discrete processes occurring, especially during later cycles. The peak at the more positive potential is the typical alloying reaction of Li with Sb. The lower potential peak is likely the same or similar reaction, though the slight shifting to lower potentials could be due to an overpotential caused by some of the active material becoming poorly electrical connected with the current collector or have its access to ions impeded by thick SEI layers. The peak potentials for delithiation of both films do not shift significantly over many cycles and capacity loss for both occurs by diminishing peak areas without significant peak shifting. This suggests that the failure mode for both films is dominated by active material loss (delamination), as capacity loss by excessive SEI that impedes ion flow would be characterized by peaks shifting to larger overpotentials.

Fig. 5d shows the specific capacity of each film as a function of cycle number, with the approximate areal capacity calculated using a nominal mass loading of ~1.26 mg/cm ^{2} for both films. For both films, the 1st lithiation capacity is significantly greater than the films' reversible capacities, as significant charge goes towards non-reversible reactions such as establishing the SEI on the electrode surface [33,34] and the poorly reversible conversion of Sb_2O_3 to Sb and Li_2O [32]. The reversible capacity of Sb@Ni stabilizes well below the theoretical capacity for Sb (660 mAh/g), and diminishes continually over 100 cycles, where the cell was stopped for post-cycling analysis. We attribute this poor performance to immediate and severe pulverization of the film, which is expected for a thick and dense film exhibiting internal stress even before cycling.

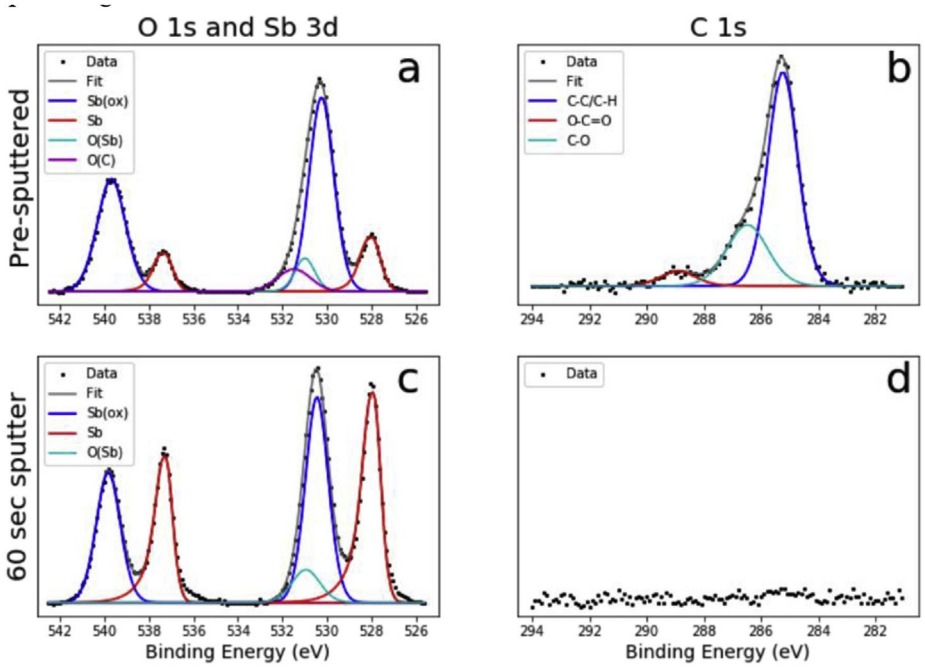

Fig. 4. XPS spectra of Sb@Ni film (a–b) before sputtering and (c–d) after 60 s of sputtering.

Additionally, because the Sb@Ni film lacks any porosity, the small reversible capacity could be limited by the large solid-state diffusion distances that Li needs to travel to access all the active material. The reversible capacity of the Sb/CNT@Ni film stabilizes above 600 mAh/g for ~60 cycles, before beginning a steady loss of capacity out to 100 cycles where the cell was stopped for post-cycling analysis. We attribute the larger reversible capacity and better stability of the Sb/CNT@Ni film compared to the Sb@Ni film to the presence of the CNTs. The embedded CNTs not only generate the porous pseudo-3D morphology of the Sb/CNT@Ni film that is more resilient to volume changes during (de) lithiation, but they also maintain mechanical and electrical connectivity to the current collector even when active material cracks. Fig. 6 shows the capacity vs. cycle number of an Sb/CNT@Ni film with higher loading (10 C/cm^2 deposition charge) that was cycled in a Li-ion half cell. The higher loading results in a smaller reversible specific capacity and less stability, showing that the reversible capacity is kinetically limited at these rates and loadings and the larger volume change of a thicker film exacerbates mechanical degradation and hastens the onset of capacity loss. Rate capability experiments of the Sb@Ni and Sb/CNT@Ni films shown in Fig. 7 also demonstrate how the inclusion of CNTs helps to maintain reversible capacity at higher cycling rates, likely due to the porosity and short solid-state diffusion distances in the Sb/CNT@Ni film.

The coulombic efficiency (CE) of both films shown in Fig. 5e identifies the low (CE) of both electrodes (99%) as a major challenge that still needs to be addressed before these electrodes can be cycled effectively in a full cell battery. The 1st cycle CE of the Sb@Ni film is 65%, which is likely due to a combination of extensive pulverization, active material loss, and SEI formation. The 1st cycle CE of the Sb/CNT@Ni film is higher, at ~78.5%, despite a larger surface area, suggesting that active material loss is not as prevalent, with SEI formation mostly contributing to the low CE. It takes about 5 cycles for each film to stabilize at higher CE values, though both remain 99%, resulting in intolerable levels of Li consumption. We attribute these low CE values to an SEI that cannot accommodate the magnitude of volume expansion of these electrode materials, and thus forms cracks in the film, exposing new surfaces that must be passivated by additional SEI on every cycle. Given that the electrolyte used for cycling these cells comprises components optimized for graphitic electrodes, the excessive SEI problem could likely be partially alleviated by developing new electrolyte additives or coatings.

Compositional quantification by EDS of the films after cycling shown in Fig. 3 reveals the presence of F and significant increase in C and O content compared to the pre-cycled films. This compositional change confirms that significant amounts of SEI are present on the films' surfaces, with the Sb/CNT@Ni film having greater amounts of SEI (larger C:Sb and O:Sb ratios) than the Sb@Ni film. Fig. 8 shows the cumulative difference between the discharge and charge capacity summed over cycle number, which we refer to as the 'excess capacity'. It is striking that the amount of excess capacity going towards SEI formation on the Sb/CNT@Ni film exceeds the reversible capacity of that film by cycle 50, despite the Sb/CNT@Ni film having the higher CE of the two for the first 50 cycles. Such an enormous amount of capacity going towards Li consuming side reactions like SEI formation would result in full cell batteries requiring significant prelithiation or excessive cathode loadings, low energy densities, and short lifetimes.

Post-cycling SEM imaging of Sb@Ni and Sb/CNT@Ni Li-ion electrodes confirms active material loss as the main mode of capacity loss for both films. Fig. 9a–b shows how the Sb@Ni electrode is severely pulverized and delaminated, which is typical of alloy anode materials with no porosity or binders. Fig. 9c–f shows how the Sb/CNT@Ni electrode is significantly delaminated but still contains large intact pieces of the film. It seems that the CNT inclusion helps to keep the active material mechanically and electrically connected. The dominant mechanism of reversible capacity loss for the Sb/CNT@Ni film seems to be active material loss through film delamination, rather than pulverization, making the substrate-film interface the weak point of the system. Work is in progress investigating strategies to improve film adhesion strength by using textured substrates or substrates with electrochemically embedded CNTs. It is striking to note that there is a significant increase in film thickness during cycling, with the film being ~5 μm before cycling (Fig. 2f) and ~30 μm after (Fig. 9f). We rationalize this 500% increase in film thickness as the filling of the film with SEI that is formed to passivate newly exposed surfaces from film cracking that occurs on every cycle. Such a large amount of SEI formation agrees with the substantial O, C, and F contents revealed by EDS in Fig. 3 and the large excess capacity shown in Fig. 8. Despite continuous SEI formation, it seems that the CNTs still maintain mechanical and electrical connectivity, allowing the film to cycle as long as it doesn't delaminate.

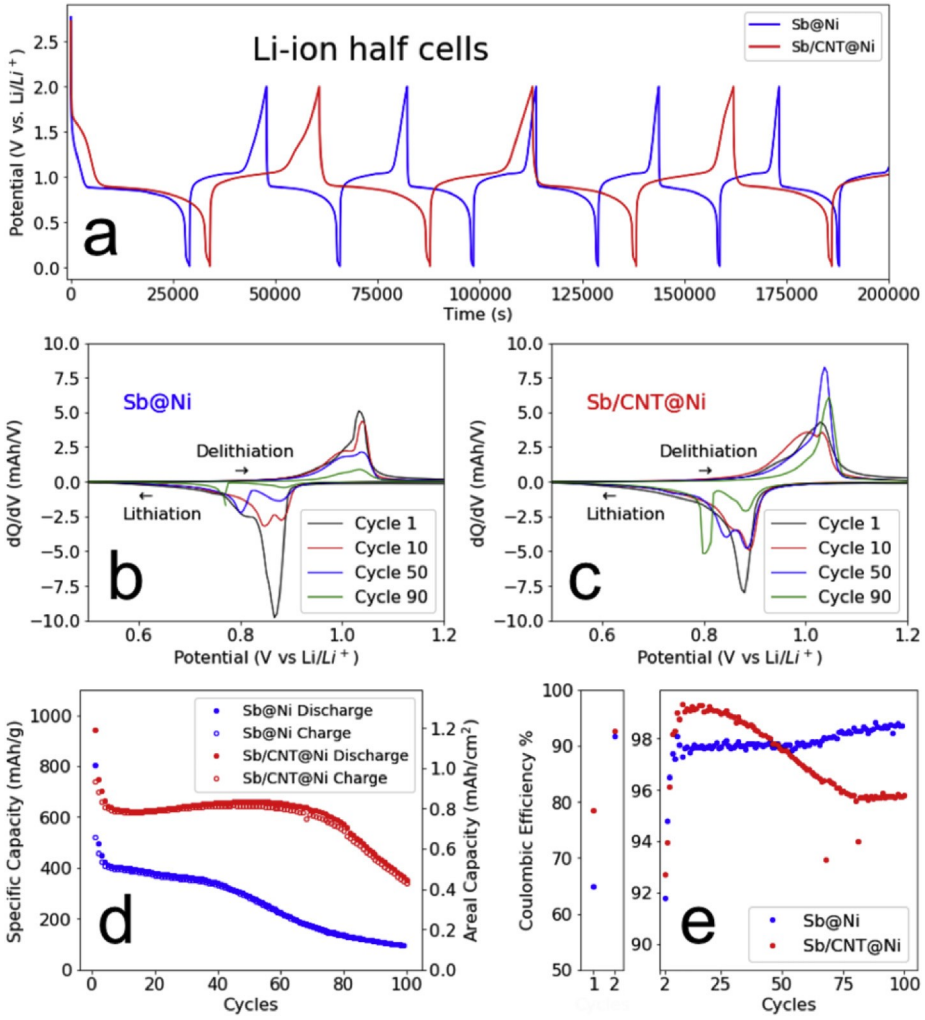

Fig. 5. Cycling data in Li-ion batteries cycled at 0.1 mA/mg: (a) Charge-discharge potential profiles and their corresponding differential capacity plots for both (b) Sb@Ni and (c) Sb/CNT@Ni electrodes in Li-ion half cells. (d) Specific capacity of both electrodes vs. cycle number and (e) their corresponding coulombic efficiencies.

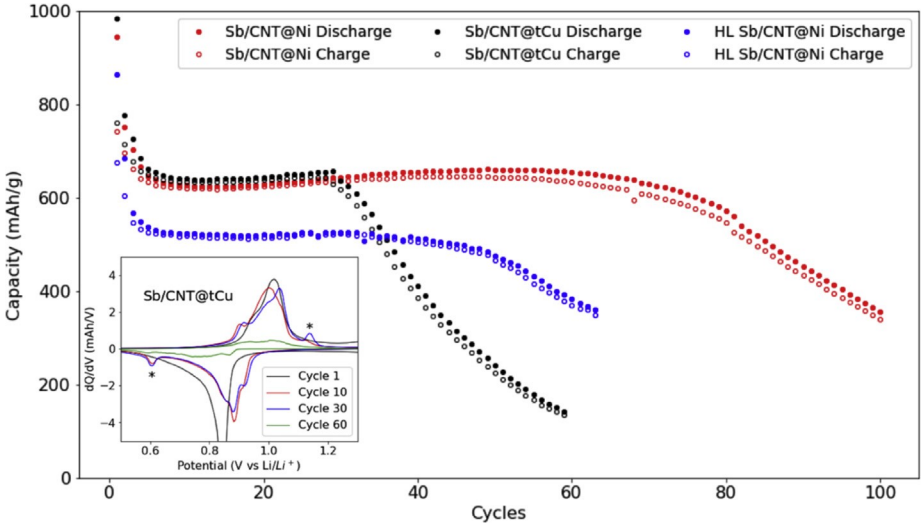

Fig. 6. Specific capacity vs. cycle number in Li-ion half cells of the following electrodes cycled at 0.1 mA/mg: (red) Sb/CNT@Ni, (black) Sb/CNT on textured Cu (Sb/CNT@tCu), (blue) and high loading (HL) of 10 C/cm^2 of electrodeposition charge Sb/CNT@Ni. The inlay shows the differential capacity of the Sb/CNT@tCu electrode for select cycles with the asterisks marking chemistry typical of Li-Cu-Sb ternary phase lithiation/delithiation, the formation of which is likely responsible for the sudden onset of capacity loss of the Sb/CNT@tCu electrode around 25 cycles. (For interpretation of the references to color in this figure legend, the reader is referred to the Web version of this article.)

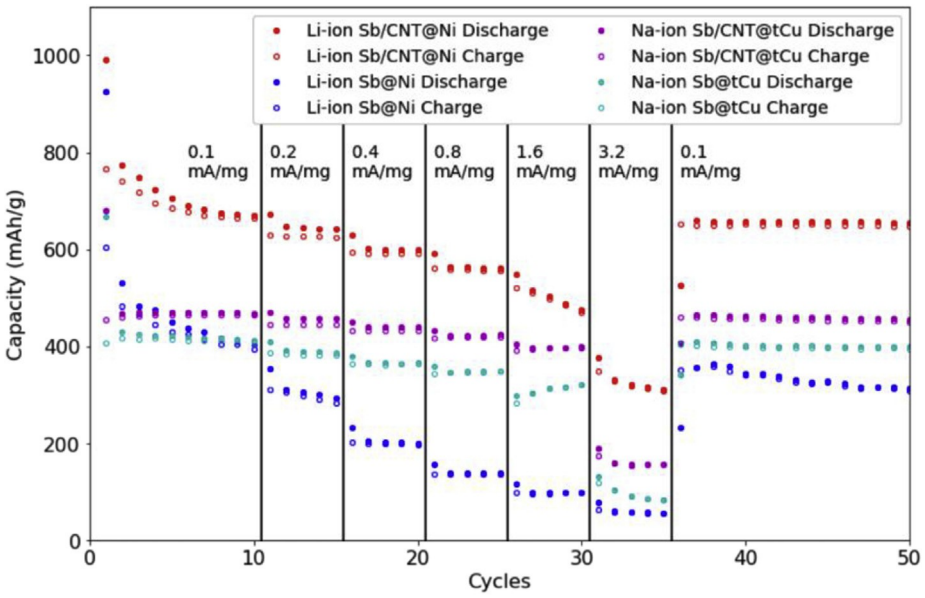

Fig. 7. Rate capability experiments for the cycling of Sb and Sb/CNT electrodes in Li-ion and Na-ion half cells.

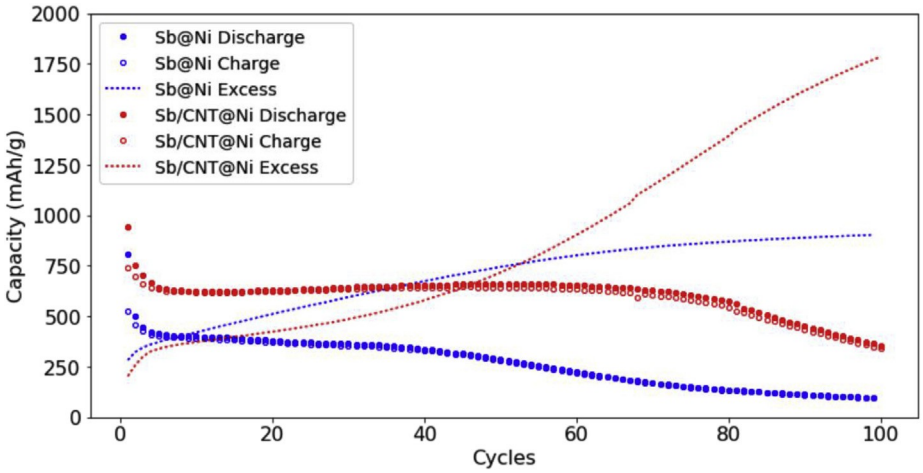

Fig. 8. Specific capacity vs. cycle number in Li-ion half cells of the following electrodes cycled at 0.1 mA/mg: (blue) Sb@Ni and (red) Sb/CNT@Ni. The dashed traces show the cumulative difference between the discharge and charge capacities and represent how much excess capacity has gone towards non-reversible electrochemistry such as SEI formation or other side reactions. The approximate trajectory mirroring of the excess capacity traces with the reversible capacity traces suggest the reversible capacity loss is due to active material loss, such as film delamination. (For interpretation of the references to color in this figure legend, the reader is referred to the Web version of this article.)

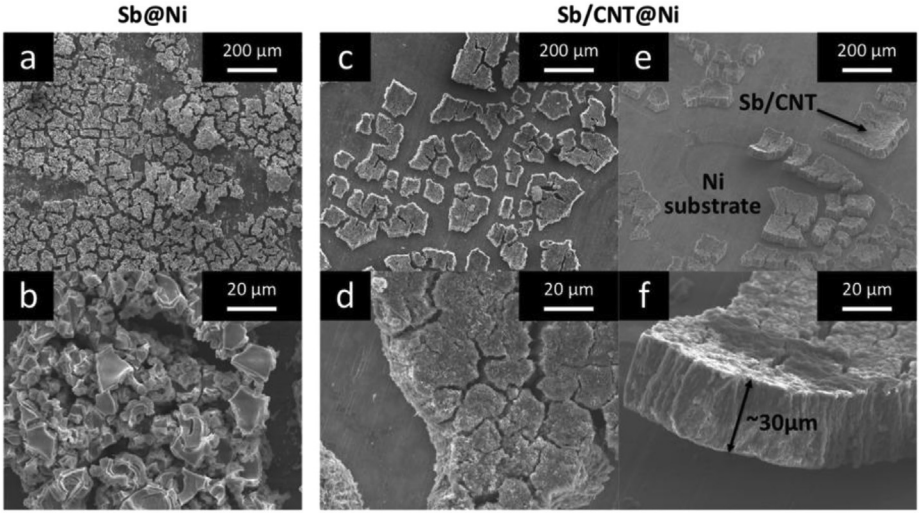

Fig. 9. SEM images of the following electrodes after being cycled in Li-ion half cells: (a–b) Sb@Ni (c–f) Sb/CNT@Ni.

3.3. Electrochemical performance of Sb and Sb/CNT composite films in Na-ion half cells

To test the electrochemical performance as Na-ion battery anodes, the Sb and Sb/CNT films were electrodeposited and galvanostatically cycled on textured Cu foils as the Sb@tCu and Sb/CNT@tCu electrodes, respectively. We chose to electrodeposit and cycle the films on Cu instead of Ni, as was done with the Li-ion half cells, because of the absence of deleterious Cu-Sb interactions when cycled in Na-ion half cells. We hypothesize that the absence of Na-Cu-Sb ternary phases makes the interdiffusion of Cu and Sb negligible during cycling in a Na-ion cell, contrary to the significant interdiffusion and void formation at Cu-Sb interfaces when cycled in a Li-ion cell, likely facilitated by the Li-Cu-Sb intermediate phases. Given that textured Cu foils are readily available and known to help adhesion of electrodeposited films [35,36], we chose them as the substrates for the films cycled in the Na-ion cells. The Sb or Sb/CNT films electrodeposited onto the textured Cu foils had no observable difference in morphology from those deposited onto flat Ni foils. As such, it is likely that the morphology of the textured Cu substrates only influences the cycling performance and failure mechanism of the films by enhancing their adhesion to the substrate, rather than changing their morphology. Fig. 11 demonstrates the early and sudden failure of an Sb/CNT@Ni film cycled in a Na-ion cell, which we attribute to film delamination from lack of film-substrate adhesion strength. Fig. 10a shows the voltage profiles for (de)sodiation of Sb@tCu and Sb/CNT@tCu, both of which are typical of Sb. Note that the Sb/CNT@tCu film exhibits less discrete potential plateaus than the Sb@tCu film, likely due to its porous and high surface area morphology where different parts of the active material are at slightly different potentials to one another during cycling. Differential capacity analysis of the potential profiles is shown for the (de)sodiation potential regions in Fig. 10b–c. For both films, the diminishing of peak areas over many cycles coincides with a significant shifting of the peaks to overpotentials. This suggests that excessive amounts of SEI form on both films that impedes (de)sodiation and contributes to active material loss as a mechanism of capacity loss.

Fig. 10d shows the specific capacity of each film as a function of cycle number, with the approximate areal capacity again calculated using a nominal mass loading of ~1.26 mg/cm ^{2} for both films. For both films, the 1st sodiation capacity is significantly greater than the films' reversible capacities, as significant charge goes towards establishing the SEI on the electrode surface [33,34]. The films stabilize at ~400 mAh/g for the Sb@tCu film and ~500 mAh/g for the Sb/CNT@tCu film upon the 1st desodiation, and both cycle stably at those capacities for >100 cycles. The Sb@tCu film starts to lose capacity rapidly around cycle 120, while the Sb/CNT@tCu begins to lose capacity slowly at around cycle 150. Both films were stopped after 190 cycles for disassembly and post-cycling

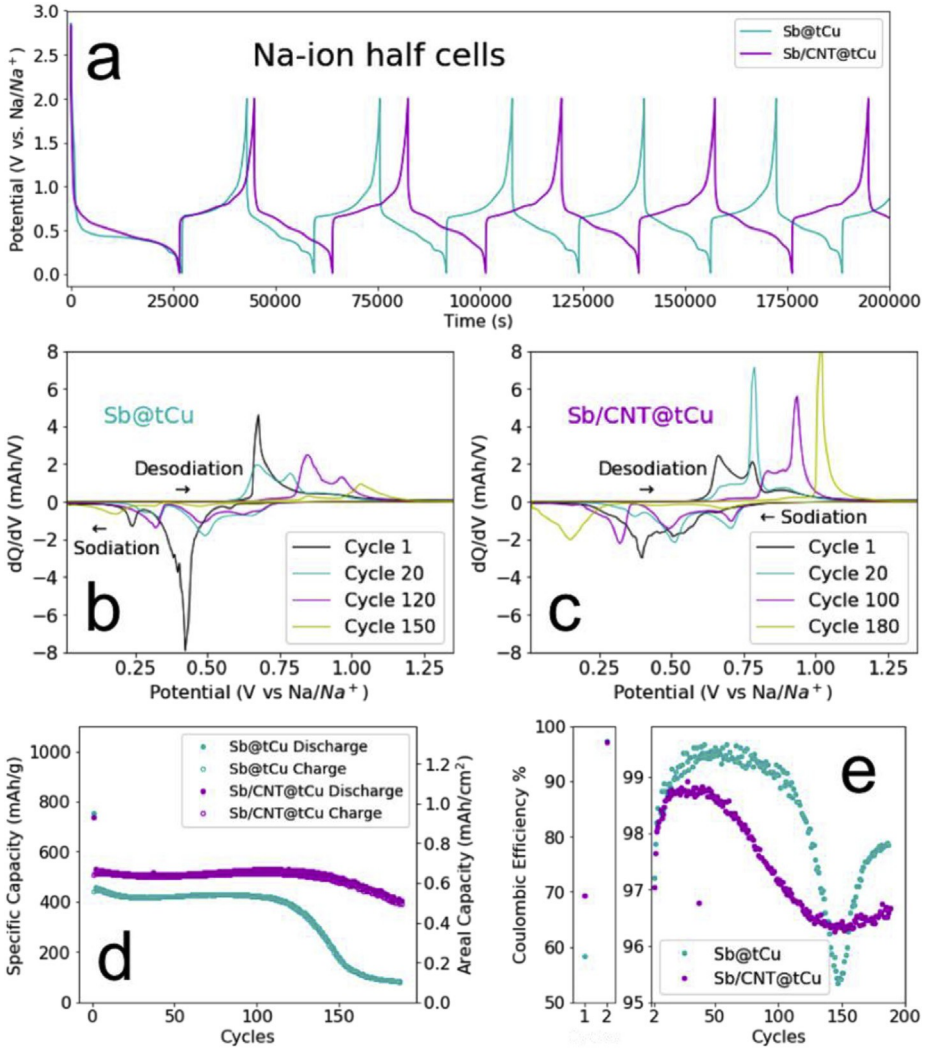

Fig. 10. Cycling data in Na-ion batteries cycled at 0.1 mA/mg: (a) Charge-discharge potential profiles and their corresponding differential capacity plots for both (b) Sb@tCu and (c) Sb/CNT@tCu electrodes in Na-ion half cells. (d) Specific capacity of both electrodes vs. cycle number and (e) their corresponding coulombic efficiencies.

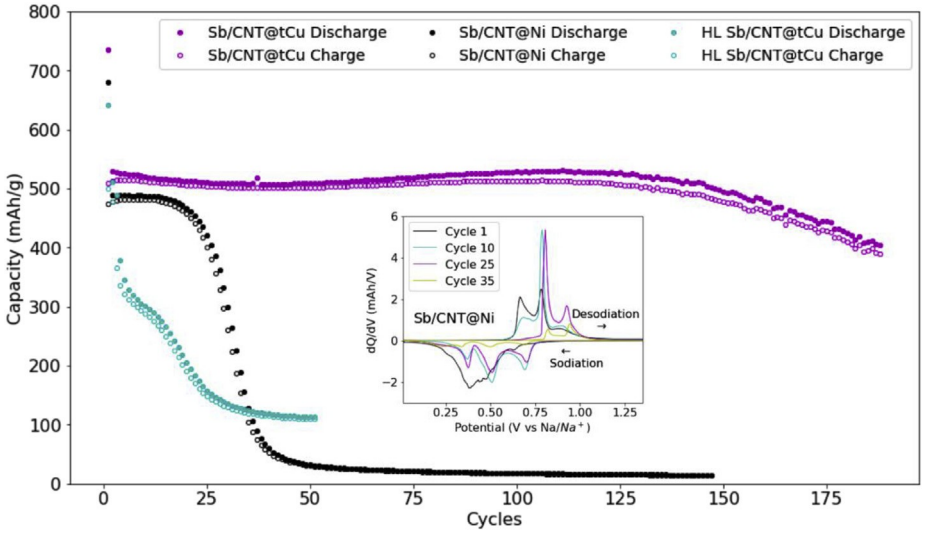

Fig. 11. Specific capacity vs. cycle number in Na-ion half cells of the following electrodes cycled at 0.1 mA/mg: (magenta) Sb/CNT@tCu, (black) Sb/CNT@Ni, (cyan) and high loading (HL) of 10 C/cm^2 of electrodeposition charge Sb/CNT@tCu. The inlay shows the differential capacity of the Sb/CNT@Ni electrode for select cycles and shows no significant difference from the differential capacity plot of the Sb/CNT@tCu electrode (Fig. 10c) other than the capacity loss manifesting as diminishment of peak area rather that peak potential shifting, suggesting capacity loss of the Sb/CNT@Ni electrode is dominated by active material delamination. The considerable capacity loss of the HL Sb/CNT@tCu indicates that the large volume expansion in the Na-ion system exacerbates delamination and capacity loss more when compared to the HL Sb/CNT@Ni electrode cycled in the Li-ion cell (Fig. 6). (For interpretation of the references to color in this figure legend, the reader is referred to the Web version of this article.)

analysis. The marginally better reversible capacity and stability of the Sb/CNT@tCu film shows that while the inclusion of the CNTs in the film is beneficial to cycling in a Na-ion cell, the benefit is not nearly as significant as in the Li-ion cells. Indeed, the rate capability experiments shown in Fig. 7 demonstrate comparable losses in reversible capacities at high cycling rates between the Sb@tCu and Sb/CNT@tCu films, showing the CNT inclusion is not beneficial to rate capability in these Na-ion electrodes. This result is somewhat unexpected considering the larger volume of Na compared to Li. However, Sb alloys with Li or Na by very different mechanisms, which has been previously shown to give bulk Sb electrodes in Na-ion batteries better cycling performance than those in Li-ion batteries. Specifically, it is thought that amorphous intermediate phases in the sodiation of Sb help relieve anisotropic strain that improves the active materials mechanical stability and rate performance [33,34]. Fig. 11 shows the capacity vs. cycle number of an Sb/CNT@tCu film with higher loading (10 C/cm^2 deposition charge) that was cycled in a Na-ion half cell. The higher loading results in extremely fast capacity loss after only 2 cycles with reversible capacities comparable to the lower loading films. The larger magnitude of volume change going from Sb → Na_3Sb compared to Sb → Li_3Sb could result in exacerbated active material loss by delamination, making a Sb/CNT film more sensitive to loading dependent stability in a Na-ion than a Li-ion cell.

The low CEs of the Na-ion cell electrodes shown in Fig. 10e are again a major challenge to be overcome. While the 1st cycle CEs for the Sb@tCu and Sb/CNT@tCu are 59% and 69%, respectively, the CE of the Sb/CNT@tCu is generally worse than that of Sb@tCu over many cycles. This might suggest that the Sb@tCu film loses more active material on the 1st cycle than the Sb/CNT@tCu film, resulting in a smaller 1st cycle CE, despite have a smaller surface area. The higher surface area of the Sb/CNT@tCu film may require more SEI formation over subsequent cycles, resulting in its CE always being <99%. Composition quantification of the films after cycling shown in Fig. 3 reveals significant amounts of SEI on both films, with the increase in C:Sb and O:Sb ratios as well as the presence of significant Na and F. Interestingly, the majority of the Sb/CNT@tCu film's composition after cycling is C and O, while the majority of the Sb@tCu film's composition after cycling is Na and F. The presence of the CNTs in the Sb/CNT@tCu film may promote the formation of an SEI with more organic speciation, compared to the more inorganic-like SEI of the Sb@tCu film after cycling. Regardless, the CE of the Sb/CNT@tCu film is too low considering the excess capacity shown in Fig. 12 exceeds the reversible capacity by around cycle 40. The intolerable levels of Na consumed in side reactions like SEI formation on every cycle would result in a full cell using this electrode material with excessive cathode loading, low energy density, and a short lifetime. The irreversible Na consumption by Sb@tCu electrode is more manageable, with the CE being 99% for ~100 cycles, resulting in the excess capacity shown in Fig. 12 being comparable to the reversible capacity for ~100 cycles. The dip in CE around cycle 150 coincides with significant capacity loss, likely from rapid active material loss as the excess capacity trace shown in Fig. 12 mirrors the decrease in reversible capacity of the Sb@tCu film.

Post-cycling SEM imaging of Sb@tCu and Sb/CNT@tCu Na-ion electrodes identifies different mechanisms of reversible capacity loss in these films. Fig. 13a–b shows some delamination of the Sb@tCu film after cycling. It is interesting to note that despite cycling stably for >100 cycles, the Sb@tCu film increased from 3.5μm (Fig. 2c) to only ~10 μm in thickness (Fig. 13b). This suggests that less SEI forms on the Sb@tCu film than the Sb/CNT@tCu film, which agrees with its comparatively smaller excess capacity shown in Fig. 12 thus making active material delamination the dominant form of reversible capacity loss in the Sb@tCu film. Additionally, the compositional quantification of the Sb@tCu film shown in Fig. 3 reveals the SEI is highly inorganic in nature with more Na and F content than C and O after cycling, which may also contribute to the compact nature of the post-cycled Sb@tCu film. Fig. 13c–f shows the Sb/CNT@tCu electrode after cycling, which exhibits negligible delamination and completely intact pieces of film present. The Sb/CNT@tCu film increased substantially in thickness, from ~5 μm before cycling (Fig. 2f) to ~60 μm after (Fig. 13f), an 1100% increase. The mechanism of this increase in film thickness is analogous to previously described, where cracks in the film fill with SEI on every cycle. The larger magnitude of thickness increase is probably a result of cycling longer and agrees with the excessively large excess capacity shown of the Sb/CNT@tCu film shown in Fig. 12. It seems the CNT inclusion as well as the textured substrate help keep the active material mechanically and electrically consolidated and well adhered. The loss in reversible capacity of the Sb/CNT@tCu is likely dominated by excessive SEI making the active material more difficult for the Na^+ to access, thus pushing the (de)sodiation events to higher overpotentials as seen in Fig. 10C.

3.4. Electrodeposition and cycling performance of Sn-Sb/CNT composite films

As a test of the applicability of this type of CNT composite electrodeposition procedure to different Li alloy anode materials, we substituted the $SbCl_3$ with $SnCl_2$ in the deposition solution and electrodeposited thin films using an analogous procedure. We chose Sn as a Li alloy material because it can be electrodeposited and exhibits larger theoretical specific capacities and lower average lithiation potentials than Sb, both of which could contribute to a higher energy density than Sb alone. Interestingly,

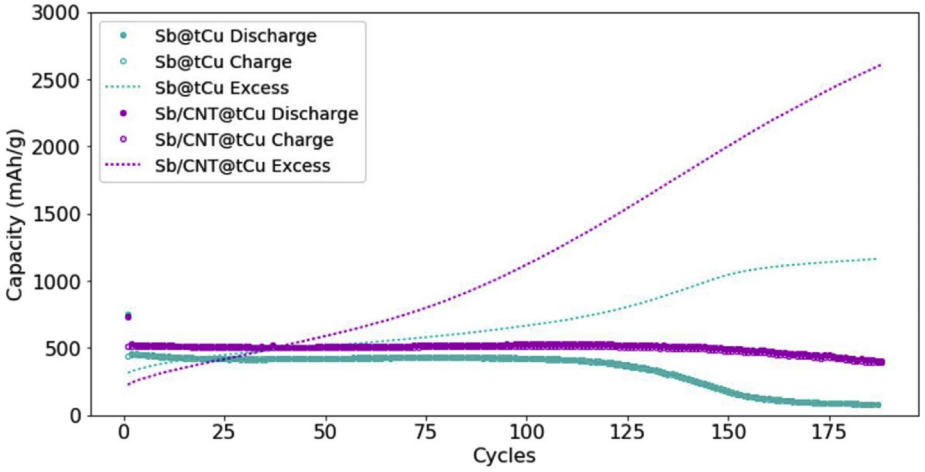

Fig. 12. Specific capacity vs. cycle number in Na-ion half cells of the following electrodes cycled at 0.1 mA/mg: (cyan) Sb@tCu and (magenta) Sb/CNT@tCu. The dashed traces show the cumulative difference between the discharge and charge capacities and represent how much excess capacity has gone towards non-reversible electrochemistry such as SEI formation or other side reactions. The close trajectory mirroring of the excess capacity trace with the reversible capacity trace of the Sb@tCu electrode suggests the reversible capacity loss of that electrode is dominated by active material loss, such as film delamination. In contrast, the continual steep increase of the excess capacity of the Sb/CNT@tCu electrode despite only a slight decline in reversible capacity suggests that the film is mechanically stable but is susceptible to excessive amounts of side reactions. (For interpretation of the references to color in this figure legend, the reader is referred to the Web version of this article.)

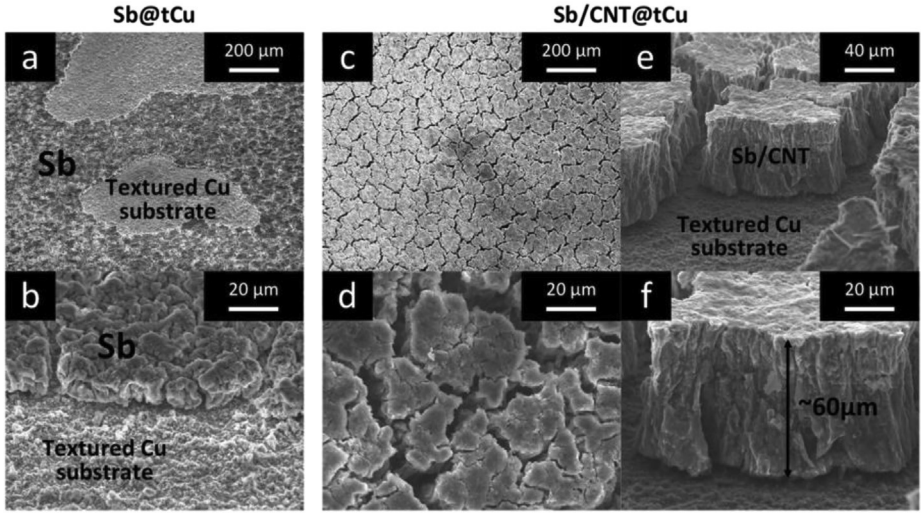

Fig. 13. SEM images of the following electrodes after being cycled in Na-ion half cells: (a–b) Sb@tCu (c–f) Sb/CNT@tCu.

the Sn/CNT@Ni film shown in Fig. 14a–b shows poor inclusion of CNTs and the absence of "beads on a string" morphology (Fig. 2e) that is

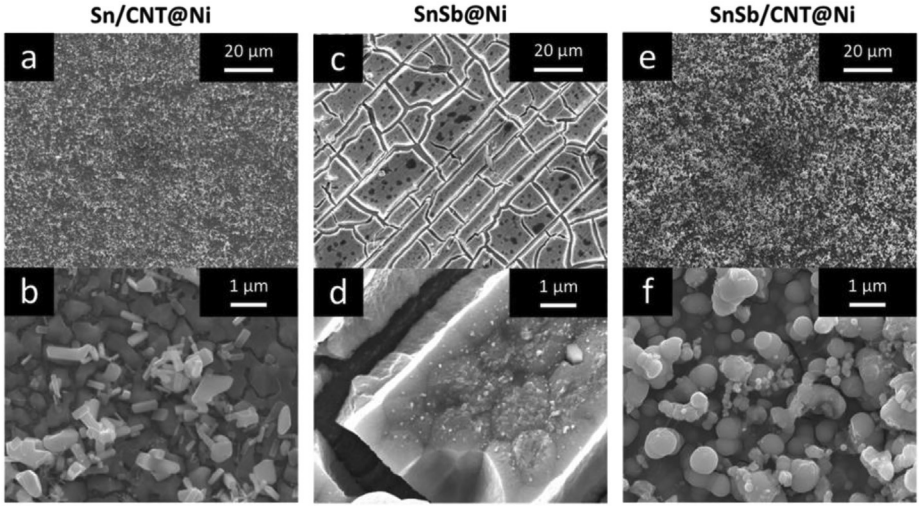

Fig. 14. SEM images of the following electrodes: (a–b) Sn/CNT@Ni deposited from a solution of 200 mM NaGluconate, 30 mM CTAB, 30 mM SnCl2, ACNTs, -1 V vs. SCE,600 s (c–d) SnSb@Ni deposited from a solution of 200 mM NaGluconate, 30 mM CTAB, 15 mM $SbCl_3$, 15 mM $SnCl_2$, -1.05 V vs. SCE,2138 mC, (e–d) SnSb/CNT@Ni deposited from a solution of 200 mM NaGluconate, 30 mM CTAB, 15 mM $SbCl_3$, 15 mM $SnCl_2$, ACNTs, 1.05 V vs. SCE, 2138 mC.

indicative of electrochemical nucleation and growth of the material onto the CNTs. By depositing from solutions with 15 mM $SbCl_3$ and 15 mM $SnCl_2$, we produced SnSb@Ni and SnSb/CNT@Ni films seen in Fig. 14c–f. The SnSb@Ni film has a composition of $Sn_{60}Sb_{40}$ as measured by EDS and exhibits cracking similar to that seen in Sb@Ni films (Fig. 2b). The SnSb/CNT@Ni film has a composition of $Sn_{47}Sb_{53}$ as measured by EDS and exhibits similar porous morphology and increased nucleation along the nanotubes as the Sb/CNT@Ni films (Fig. 2e). It seems that the presence of Sb is required to achieve good integration of CNTs and promote the deposition along the nanotubes, a phenomenon that may be worth investigating more closely.

The electrochemical performance of SnSb@Ni and SnSb/CNT@Ni films as Li-ion battery anodes was assessed by galvanostatically cycling the films in Li-ion half cells. Fig. 15a shows the voltage profiles for (de)lithiation of the SnSb@Ni and SnSb/CNT@Ni. For both, the presence of Sn contributes a significant amount of capacity below 0.75 V and 0.9 V vs. Li/Li^+ for the lithiation and delithiation, respectively, when compared to the cycling of the Sb@Ni or Sb/CNT@Ni films in Fig. 5a. Similarly to the Sb/CNT@Ni film, the SnSb/CNT@Ni film also passes more current above 1.2 V vs. Li/Li^+ than the SnSb@Ni film due to the higher surface area of the CNT composite. The differential capacity plots (Fig. 15b–c) also differ significantly from the pure Sb films (Fig. 5b–c), with the SnSb films exhibiting more electrochemical events at lower potentials due to the (de)lithiation of Sn. The specific capacity and coulombic efficiency as a function of cycle number for both the SnSb@Ni and SnSb/CNT@Ni are shown in Fig. 15d–e. They show an analogous improvement in cycling stability due to the inclusion of the CNTs, with the SnSb/CNT@Ni film cycling around 600 mAh/g for around 75 cycles while the SnSb@Ni film begins losing significant capacity within the first few cycles and exhibits negligible reversible capacity by cycle 50. The much faster degradation of SnSb@Ni film compared to the Sb@Ni film is likely due to the presence of Sn grains in the deposit, which has been shown to be detrimental for capacity retention in SnSb anodes for Na-ion batteries [37]. Post cycling analysis of the films by SEM (not shown) identifies active material loss by delamination as the ultimate failure mode for both films, though it occurs much more rapidly in the SnSb@Ni film. The SnSb/CNT@Ni film also exhibits a near 10-fold increase in film thickness during cycling, indicating the formation of excessive amounts of SEI that agrees with its low coulombic efficiencies shown in Fig. 15e. While it is clear that the electrodeposition of CNT composite films of other alloy materials like SnSb is an effective strategy to improve cycling stability in Li-ion batteries, the composite films still suffer from the main failure modes of delamination and, more importantly, unacceptably low coulombic efficiency. Anode failure by delamination or other mechanical degradations could be alleviated by electrodeposition of films that are locally thinner, using high surface area substrates like 3D scaffolds to achieve the high active material loadings desired. Ultimately, the low coulombic efficiency of these electrodes is the most important failure

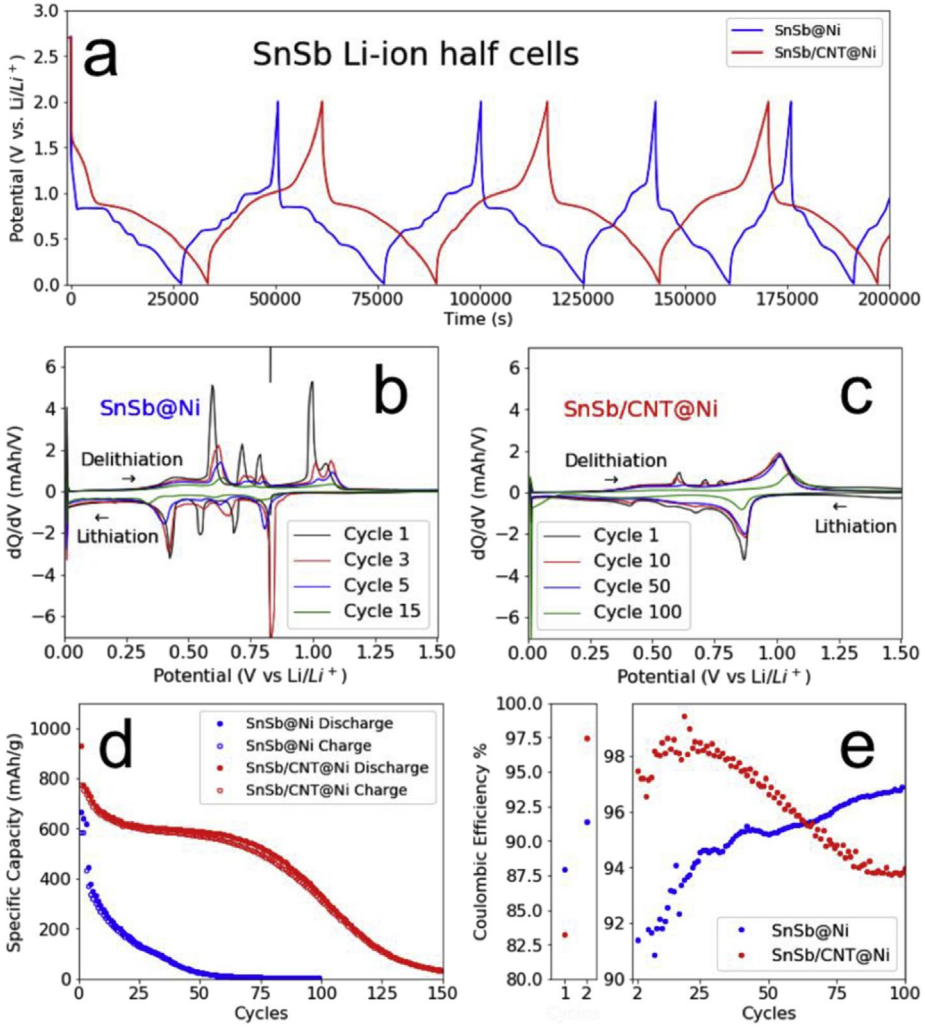

Fig. 15. Cycling data of SnSb electrodes in Li-ion batteries cycled at 0.1 mA/mg: (a) Charge-discharge potential pro files and their corresponding differential capacity plots for both (b) SnSb@Ni and (c) SnSb/CNT@Ni electrodes in Li-ion half cells. (d) Speci fic capacity of both electrodes vs. cycle number and (e) their corresponding coulombic efficiencies.

mode that will have to be solved by using better developed electrolyte additives or flexible electrode coatings, for example.

4. Conclusion

Towards the goal of creating batteries with higher energy density, better safety, and longer lifetimes, we have demonstrated the application of performance improving strategies to make Sb/CNT composite anodes for Li and Na-ion batteries. The Sb/CNT composite anodes can be electrodeposited from aqueous mixtures, making the synthesis of these types of anodes commercially feasible and applicable to non-planar (3D) electrode architectures. When cycled in Li-ion and Na-ion half-cells, the composite anodes exhibit larger reversible capacities and longer cycle lifetimes than anodes without CNTs, an improvement that is more substantial in the Li-ion cells. We attribute the better performance of the composite anodes to the mechanical and electrical connectivity that the CNTs provide as well as the porous morphology that results from CNT incorporation. Post-cycling characterization of the composite anodes reveals different modes for reversible capacity loss between the Li-ion and Na-ion cells. The Li-ion anodes suffer mainly from active material loss in the form of film delamination from the substrate. The Na-ion anodes exhibit improved film-substrate adhesion, in large part from the textured substrate used, though lose reversible capacity as excessive amounts of SEI build-up around the active material. We additionally demonstrated that the electrodeposition of CNT composite anodes could be extended to other alloy active materials, namely SnSb/CNT composites. This work successfully demonstrates that the incorporation of CNTs improves the mechanical and electrical connectivity of the composite electrodes' active material, resulting in extended cycle lifetimes of those electrodes in both Li-ion and Na-ion half-cells. This is a key work in conjunction with efforts to develop better electrolyte additives, electrode coatings, or solid electrolytes to address the low coulombic efficiencies (<99%) of these types of electrodes so they can be used effectively in full-cell batteries.

Declarations of interest

None.

Data availability statement

The raw/processed data required to reproduce these findings can be obtained by contacting the corresponding author directly.

Acknowledgements

The authors thank Dr. Pat McCurdy (Central Instrumentation Facility) for assistance with the SEM–EDS. This work was supported through the NSF SSMC program (SSMC-1710672) and RMB was supported by CHE-1339674 for C-CLEAR.

Appendix A. Supplementary data

Supplementary data to this article can be found online at https://doi.org/10.1016/j.ensm.2019.09.025.

References

[1] T.M. Gür, Review of electrical energy storage technologies, materials and systems: challenges and prospects for large-scale grid storage, Energy Environ. Sci. 11 (2018) 2696–2767, https://doi.org/10.1039/C8EE01419A.
[2] J.B. Goodenough, Energy storage materials_ A perspective, Energy Storage Mater. 1 (2015) 158–161, https://doi.org/10.1016/j.ensm.2015.07.001.
[3] J. Meng, H. Guo, C. Niu, Y. Zhao, L. Xu, Q. Li, et al., Advances in structure and property optimizations of battery electrode materials, Joule 1 (2017) 522–547, https://doi.org/10.1016/j.joule.2017.08.001.
[4] M.N. Obrovac, V.L. Chevrier, Alloy negative electrodes for Li-ion batteries, Chem. Rev. 114 (2014) 11444–11502, https://doi.org/10.1021/cr500207g.
[5] C. Delmas, Sodium and Sodium-Ion Batteries: 50 Years of Research, 29, 2018, pp. 1703137–1703139, https://doi.org/10.1002/aenm.201703137.
[6] J.-Y. Hwang, S.-T. Myung, Y.-K. Sun, Sodium-ion batteries: present and future, Chem. Soc. Rev. 334 (2017) 928, https://doi.org/10.1039/C6CS00776G.
[7] M. Winter, The solid electrolyte interphase – the most important and the least understood solid electrolyte in rechargeable Li batteries, Z. Phys. Chem. 223 (2009) 1395–1406, https://doi.org/10.1524/zpch.2009.6086.
[8] C.K. Chan, R. Ruffo, S.S. Hong, Y. Cui, Surface chemistry and morphology of the solid electrolyte interphase on silicon nanowire lithium-ion battery anodes, J. Power Sources 189 (2009) 1132–1140, https://doi.org/10.1016/j.jpowsour.2009.01.007.
[9] K. Xu, Nonaqueous Liquid Electrolytes for Lithium-Based Rechargeable Batteries, 104, 2004, pp. 4303–4417, https://doi.org/10.1021/cr030203g.
[10] Z. Liu, T. Song, U. Paik, Sb-based electrode materials for rechargeable batteries, J. Mater. Chem.: Mater. Energy Sustain. 6 (2018) 8159–8193, https://doi.org/10.1039/C8TA01782D.
[11] R. Al-Salman, S.J. Sedlmaier, H. Sommer, T. Brezesinski, J. Janek, Facile synthesis of micrometer-long antimony nanowires by template-free electrodeposition for next generation Li-ion batteries, J. Mater. Chem. A. 4 (2016) 12726–12729, https://doi.org/10.1039/C6TA04731A.
[12] J. He, Y. Wei, T. Zhai, H. Li, Antimony-based materials as promising anodes for rechargeable lithium-ion and sodium-ion batteries, Mater. Chem. Front. 2 (2018) 437–455, https://doi.org/10.1039/C7QM00480J.
[13] E.D. Jackson, J.M. Mosby, A.L. Prieto, Evaluation of the electrochemical properties of crystalline copper antimonide thin film anodes for lithium ion batteries produced by single step electrodeposition, Electrochim. Acta 214 (2016) 253–264, https://doi.org/10.1016/j.electacta.2016.07.126.
[14] M.C. Schulze, R.K. Schulze, A.L. Prieto, Electrodeposited thin-film Cu_xSb anodes for Li-ion batteries: enhancement of cycle life via tuning of film composition and engineering of the film-substrate interface, J. Mater. Chem. A. 6 (2018) 12708–12717, https://doi.org/10.1039/C8TA01798K.
[15] J.M. Mosby, A.L. Prieto, Direct electrodeposition of Cu 2Sb for lithium-ion battery anodes, J. Am. Chem. Soc. 130 (2008) 10656–10661, https://doi.org/10.1021/ja801745n.
[16] E.D. Jackson, A.L. Prieto, Copper antimonide nanowire array lithium ion anodes stabilized by electrolyte additives, ACS Appl. Mater. Interfaces 8 (2016) 30379–30386, https://doi.org/10.1021/acsami.6b08033.
[17] S.-K. KIM, T.-S. OH, Electrodeposition behavior and characteristics of Ni-carbon nanotube composite coatings, Trans. Nonferrous Metals Soc. China 21 (2011) s68–s72, https://doi.org/10.1016/S1003-6326(11)61063-7.
[18] S. Arai, Y. Suwa, M. Endo, Cu/Multiwalled carbon nanotube composite films fabricated by pulse-reverse electrodeposition, J. Electrochem. Soc. 158 (2011) D49–D53, https://doi.org/10.1149/1.3518414.
[19] P.-M. Hannula, A. Peltonen, J. Aromaa, D. Janas, M. Lundström, B.P. Wilson, et al., Carbon nanotube-copper composites by electrodeposition on carbon nanotube fibers, Carbon 107 (2016) 281–287, https://doi.org/10.1016/j.carbon.2016.06.008.
[20] S. Arai, M. Endo, Carbon nanofiber-copper composites fabricated by electroplating, Electrochem. Solid State Lett. 7 (2004) C25–C26, https://doi.org/10.1149/1.1644354.
[21] B.J. Landi, M.J. Ganter, C.D. Cress, R.A. DiLeo, R.P. Raffaelle, Carbon nanotubes for lithium ion batteries, Energy Environ. Sci. 2 (2009) 638–654, https://doi.org/10.1039/b904116h.
[22] S.-W. Kim, D.T. Ngo, J. Heo, C.-N. Park, C.-J. Park, Electrodeposited germanium/carbon composite as an anode material for lithium ion batteries, Electrochim. Acta 238 (2017) 319–329, https://doi.org/10.1016/j.electacta.2017.04.027.
[23] M. Uysal, T. Cetinkaya, A. Alp, H. Akbulut, Production of Sn/MWCNT nanocomposite anodes by pulse electrodeposition for Li-ion batteries, Appl. Surf. Sci. 290 (2014) 6–12, https://doi.org/10.1016/j.apsusc.2013.10.162.
[24] J.H. Lee, B.-S. Kong, S.B. Yang, H.-T. Jung, Fabrication of single-walled carbon nanotube/tin nanoparticle composites by electrochemical reduction combined with vacuum filtration and hybrid co-filtration for high-performance lithium battery electrodes, J. Power Sources 194 (2009) 520–525, https://doi.org/10.1016/j.jpowsour.2009.04.045.
[25] C. Sotowa, G. Origi, M. Takeuchi, Y. Nishimura, K. Takeuchi, I.Y. Jang, et al., The reinforcing effect of combined carbon nanotubes and acetylene blacks on the positive electrode of lithium-ion batteries, ChemSusChem 1 (2008) 911–915, https://doi.org/10.1002/cssc.200800170 .
[26] X. Liu, Y. Du, X. Xu, X. Zhou, Z. Dai, J. Bao, Enhancing the anode performance of antimony through nitrogen-doped carbon and carbon nanotubes, J. Phys. Chem. C 120 (2016) 3214–3220, https://doi.org/10.1021/acs.jpcc.5b11926.
[27] M. Alaf, H. Akbulut, Electrochemical energy storage behavior of Sn/SnO2 double phase nanocomposite anodes produced on the multiwalled carbon nanotube buckypapers for lithium-ion batteries, J. Power Sources 247 (2014) 692–702, https://doi.org/10.1016/j.jpowsour.2013.09.020.
[28] L.-F. Cui, L. Hu, J.W. Choi, Y. Cui, Light-weight free-standing carbon nanotube-silicon films for anodes of lithium ion batteries, ACS Nano 4 (2010) 3671–3678, https://doi.org/10.1021/nn100619m.
[29] D.L. Wood, J.D. Quass, J. Li, S. Ahmed, D. Ventola, C. Daniel, Technical and economic analysis of solvent-based lithium-ion electrode drying with water and NMP, Dry. Technol. 36 (2017) 234–244, https://doi.org/10.1080/07373937.2017.1319855.
[30] E.F. de la Cruz, Y. Zheng, E. Torres, W. Li, W. Song, K. Burugapalli, Zeta potential of modified multi-walled carbon nanotubes in presence of poly (vinyl alcohol) hydrogel, Int. J. Electrochem. Sci. 7 (2012) 3577–3590.

[31] J. Sun, L. Gao, W. Li, Colloidal processing of carbon nanotube/alumina composites, Chem. Mater. 14 (2002) 5169–5172, https://doi.org/10.1021/cm020736q.
[32] Hanna Bryngelsson, Jonas Eskhult, Leif Nyholm, Merja Herranen, A. Oscar Alm, K. Edstr6m, Electrodeposited Sb and Sb/Sb2O3 nanoparticle coatings as anode materials for Li-ion batteries, Chem. Mater. 19 (2007) 1170–1180, https://doi.org/10.1021/cm0624769.
[33] A. Darwiche, C. Marino, M.T. Sougrati, B. Fraisse, L. Stievano, L. Monconduit, Better cycling performances of bulk Sb in Na-ion batteries compared to Li-ion systems: an unexpected electrochemical mechanism, J. Am. Chem. Soc. 134 (2012) 20805–20811, https://doi.org/10.1021/ja310347x.
[34] M. He, K. Kravchyk, M. Walter, M.V. Kovalenko, Monodisperse antimony nanocrystals for high-rate Li-ion and Na-ion battery anodes: nano versus bulk, Nano Lett. 14 (2014) 1255–1262, https://doi.org/10.1021/nl404165c.
[35] J. Park, S. Rajendran, H. Kwon, Effects of substrate morphology and ageing on cycle performance of a Sn-anode fabricated by electroplating, J. Power Sources 159 (2006) 1409–1415, https://doi.org/10.1016/j.jpowsour.2005.11.064.
[36] N.-R. Shin, Y.-M. Kang, M.-S. Song, D.-Y. Kim, H.-S. Kwon, Effects of Cu substrate morphology and phase control on electrochemical performance of Sn–Ni alloys for Li-ion battery, J. Power Sources 186 (2009) 201–205, https://doi.org/10.1016/j.jpowsour.2008.09.095.
[37] J. Ma, A.L. Prieto, Electrodeposition of pure phase SnSb exhibiting high stability as a sodium-ion battery anode, Chem. Commun. 55 (2019) 6938–6941, https://doi.org/10.1039/C9CC00001A.